



Validation simulations for the variational approach to fracture

A. Mesgarnejad^a, B. Bourdin^{b,*}, M.M. Khonsari^a

^aDepartment of Mechanical and Industrial Engineering, Louisiana State University, Baton Rouge, LA 70803, USA

^bDepartment of Mathematics and Center for Computation & Technology, Louisiana State University, Baton Rouge, LA 70803, USA

Received 10 August 2014; received in revised form 26 October 2014; accepted 31 October 2014

Available online 17 November 2014

Abstract

In this article, we focus on the validation of Francfort and Marigo's variational approach to fracture based on some classical fracture experiments. We show that this approach can be used to faithfully account for unknown crack paths even for complex loadings and geometry. We revisit the backtracking algorithm, aimed at avoiding some spurious local minimizers of the total fracture energy and introduce a variant: the deep backtracking algorithm.

© 2014 Elsevier B.V. All rights reserved.

Keywords: Variational approach to fracture; Brittle fracture; Validation; Phase-field methods

1. Introduction

The modeling of crack geometry (path) has been one of the most challenging and elusive aspects of fracture mechanics and has captured the interest of scientists in different disciplines for many years. The difficulty in this endeavor is two-fold: deriving proper models capable of predicting potentially complex unknown crack paths, and coming up with numerical schemes capable of dealing with the unknown crack geometry without remeshing. The later issue has been tackled with some success by methods based on enriching the approximation space through cohesive [1,2] or extended [3,4] finite elements, or non-local approximations based on phase-fields [5–7], level sets [8,9] or eigendecomposition [10].

Francfort and Marigo's variational approach to fracture [11–13] aims at addressing both issues simultaneously by providing a rigorous model derived from Griffith's concept of energy restitution between bulk and surface energies, and providing an efficient numerical implementation capable of handling complex unknown crack path. Over the last decade, this approach was applied to many areas including elastic fracture [12,14,15], thermoelastic fracture [16,17], thin-film fracture [18–20], thin-shells [21], electro-mechanical fracture [22,23], or dynamic fracture [24–27] to name a few. A major difficulty associated with the variational approach to fracture is the reliance on global energy minimization, which can sometimes result in unrealistic crack paths by making equally admissible “near” and “far” points in configuration space. In this paper, we propose a variant of the backtracking algorithm from [15] that allows a more

* Corresponding author.

E-mail addresses: amesga1@tigers.lsu.edu (A. Mesgarnejad), bourdin@lsu.edu (B. Bourdin), khonsari@me.lsu.edu (M.M. Khonsari).

thorough exploration of “near” states. While most of the literature focuses on verification simulations, or numerical investigations of the properties of such models or algorithms, we focus on the quantitative validation of our method. We use available well-documented experimental data to illustrate the ability of this deep backtracking algorithm, combined with the regularized expression of the variational fracture energy to accurately predict crack paths in realistic situations.

We begin this paper by providing a brief a review of the variational fracture mechanics framework in Section 2. In Section 3, we review its approximation and minimization processes and introduce the deep backtracking algorithm. In Section 4, we compare numerical simulations with experimental results. Finally in Section 5, we summarize different aspects of the results obtained in this article.

2. Methodology

2.1. The variational approach to elastic fracture

The foundation of the variational approach to fracture mechanics is to associate a potential energy consisting of the stored elastic energy, the work of external forces, and the energy dissipated through fracture to any crack and deformation configuration of a brittle body. For a body occupying a reference configuration $\Omega \subset \mathbb{R}^n$, $n = 2$ or 3 , subject to a displacement u and containing the set of cracks $\Gamma \subset \Omega$, we define the potential energy $\mathcal{E}_I(u, \Gamma)$ as:

$$\mathcal{E}_I(u, \Gamma) := \mathcal{P}_I(u, \Gamma) + \mathcal{S}(\Gamma) \tag{1}$$

where $\mathcal{P}_I(u, \Gamma)$ is the deformation energy stored in the body and $\mathcal{S}(\Gamma)$ is the energy dissipated through fracture (*i.e.*, the surface energy). The mechanical energy can be written in terms of its local potential $\mathcal{W}(u)$ and the work of the external forces f_t acting on a part $\partial_N \Omega$, of the boundary of the domain

$$\mathcal{P}_I(u, \Gamma) := \frac{1}{2} \int_{\Omega \setminus \Gamma} \mathcal{W}(e(u)) \, dx - \int_{\partial_N \Omega} f_t \cdot u \, dx. \tag{2}$$

In all that follows, we consider linear elastic materials so that

$$\mathcal{W}(e(u)) := \mathbb{C} e(u) : e(u) \tag{3}$$

where \mathbb{C} is the fourth order elastic constitutive tensor and $e(u) := (\nabla u + \nabla u^T)/2$ is the linear elastic strain (*i.e.*, the symmetric gradient). For brittle materials, we define the surface energy, $\mathcal{S}(\Gamma)$ as:

$$\mathcal{S}(\Gamma) := G_c \mathcal{H}^{n-1}(\Gamma) \tag{4}$$

where G_c is the energy required to create a unit area (unit length) of new cracks, \mathcal{H}^m is the m -dimensional Hausdorff measure (*i.e.*, $\mathcal{H}^2(\Gamma)$ is the aggregate area and $\mathcal{H}^1(\Gamma)$ is the aggregate length of cracks Γ in three and two dimensions respectively).

2.2. Non-dimensionalization

To carry out the computations, we introduce a reference displacement u_0 , a reference length L_0 , a reference stress E_0 , and define the non-dimensional displacement \tilde{u} , coordinates \tilde{x} , elastic constitutive tensor $\tilde{\mathbb{C}}$, and force \tilde{f}_t as:

$$\begin{aligned} \tilde{u} &:= \frac{u}{u_0}, \\ \tilde{x} &:= \frac{x}{L_0}, \\ \tilde{\mathbb{C}} &:= \frac{\mathbb{C}}{E_0}, \\ \tilde{f}_t &:= \frac{f_t}{E_0}. \end{aligned}$$

We then define the n -dimensional non-dimensional potential energy

$$\begin{aligned} \tilde{\mathcal{E}}(\tilde{u}, \tilde{\Gamma}) &:= \frac{1}{E_0 u_0^2 L_0^{n-2}} \mathcal{E}(u, \Gamma) \\ &= \frac{1}{2} \int_{\tilde{\Omega} \setminus \tilde{\Gamma}} \tilde{\mathbb{C}} \tilde{\boldsymbol{\epsilon}}(\tilde{u}) : \tilde{\boldsymbol{\epsilon}}(\tilde{u}) \, d\tilde{x} - \int_{\partial_N \tilde{\Omega}} \frac{L_0}{u_0} \tilde{f}_t \cdot \tilde{u} \, d\tilde{x} + \frac{G_c L}{E_0 u_0^2} \mathcal{H}^{n-1}(\tilde{\Gamma}). \end{aligned} \tag{5}$$

It is then natural to define a non-dimensional fracture toughness \tilde{G}

$$\tilde{G} := \frac{G_c L_0}{E_0 u_0^2}, \tag{6}$$

so that the non-dimensional total energy (5) becomes:

$$\tilde{\mathcal{E}}_t(\tilde{u}, \tilde{\Gamma}) = \frac{1}{2} \int_{\tilde{\Omega} \setminus \tilde{\Gamma}} \tilde{\mathbb{C}} \tilde{\boldsymbol{\epsilon}}(\tilde{u}) : \tilde{\boldsymbol{\epsilon}}(\tilde{u}) \, d\tilde{x} - \int_{\partial_N \tilde{\Omega}} \tilde{f}_t \cdot \tilde{u} \, d\tilde{x} + \tilde{G} H^{n-1}(\tilde{\Gamma}). \tag{7}$$

For ease in notation, from this point on we omit the tilde on all fields, *i.e.*, we write u for \tilde{u} and so on.

2.3. Quasi-static evolution

In this article we focus on a quasi-static evolution of fracture. For a crack set Γ , the admissible displacement set consists of functions $\mathcal{K}_t(\Gamma) := \{u \in H^1(\Omega \setminus \Gamma, \mathbb{R}^n) \mid u(x) = \bar{u}_t(x), \forall x \in \partial_D \Omega\}$, where $\bar{u}_t(x)$ is a given prescribed boundary displacement on a part $\partial_D \Omega$ of $\partial \Omega$ disjoint from $\partial_N \Omega$. Following [13], the evolution of the displacement field and associated crack set for a given loading history f_t (and boundary conditions \bar{u}_t) is given by the continuous evolution law:

Definition 1 (*Quasi-static Evolution*). Given a loading sequence (f_t, \bar{u}_t) for $t \in [0, t_{\max}]$, a function $t \rightarrow (u_t \in \mathcal{K}_t(\Gamma_t), \Gamma_t \subset \bar{\Omega})$ is the solution of the quasi-static evolution if it satisfies:

- **(IR)** Irreversibility of the crack evolution:

$$\Gamma_t \supseteq \Gamma_s, \quad \forall 0 \leq s \leq t \tag{8}$$

- **(GST)** Unilateral global minimality: At any time $t \in [0, t_{\max}]$, the state (u_t, Γ_t) is such that:

$$\mathcal{E}_t(u_t, \Gamma_t) \leq \mathcal{E}_t(u, \Gamma), \quad \forall u \in \mathcal{K}_t(\Gamma_t), \quad \forall \Gamma \supseteq \Gamma_t \tag{9}$$

- **(EB)** Energy balance: the function $\mathcal{E}(t) := \mathcal{E}_t(u_t, \Gamma_t)$ is absolutely continuous in t and satisfies the condition

$$\frac{d\mathcal{E}}{dt} = \int_{\partial_D \Omega \setminus \Gamma(t(t))} \nabla \mathcal{W}(\mathbf{e}(u_t)) \cdot \dot{u}_t \, dx - \int_{\partial_N \Omega} \dot{f}_t \cdot u_t \, ds. \tag{10}$$

Since evolution in time is only accounted through the irreversibility condition the formulation here is rate-independent; therefore, up to a rescaling of time, any monotonically increasing load can be replaced with a linear scaling of a reference load

$$f_t = t f_0 \tag{11}$$

where the parameter t is merely a scaling factor. We nevertheless refer to t as “time”.

2.4. Approximation of the energy functional

The implementation of the variational approach to fracture requires the use of sophisticated numerical algorithms. Specifically, the minimization of the displacement field with respect to any kinematically admissible displacement and any set of crack curves introduces a high level of complexity. We follow the approach presented in-depth in [13] and references therein. We introduce a regularization parameter $\epsilon > 0$ homogeneous to a length and a secondary variable α taking its values in $(0, 1)$ to represent the cracks. We define the regularized energy

$$\mathcal{E}_{t,\epsilon}(u, \alpha) := \mathcal{P}_t(u, \alpha) + \mathcal{S}_\epsilon(\alpha), \tag{12}$$

where

$$\mathcal{P}_t(u, \alpha) := \frac{1}{2} \int_{\Omega} (1 - \alpha)^2 \mathbb{C}e(u) : e(u) \, dx - \int_{\partial_N \Omega} f_i \cdot u_t \, ds, \tag{13}$$

and the fracture (surface) energy as:

$$\mathcal{S}_{\epsilon}(\alpha) := \frac{G_c}{4C_v} \int_{\Omega} \frac{V(\alpha)}{\epsilon} + \epsilon |\nabla \alpha|^2 \, dx, \tag{14}$$

where

$$C_v = \int_0^1 \sqrt{V(\alpha)} \, d\alpha \tag{15}$$

is a normalization constant (see [28] for instance). The specific choice of the dissipation potential $V(\alpha) = \alpha$ is motivated by the convenience of its numerical implementation and the specific properties of the model at fixed ϵ , namely a stress-softening behavior with an elastic domain [29,30].

The form of the regularized energy (12) is motivated by a now large body of theoretical work establishing it as an approximation, in the sense of Γ -convergence, of the fracture energy \mathcal{E}_t [31–36]. Roughly speaking, as $\epsilon \rightarrow 0$, the displacement field minimizing (12) converges to that of minimizing (1), the field α converges to 0 almost everywhere and goes to zero “near the jumps of u ” (*i.e.*, the cracks).

In our numerical simulations, we consider a time discretization of the quasi-static evolution: we introduce a discrete set of loading parameters $0 = t_0 \leq \dots \leq t_N = t_{\max}$ and for a given choice of the regularization parameter ϵ , we seek minimizers of the regularized energy. At each time step, the irreversibility condition is accounted for through the addition of constraints on the field α . Namely, for each t_i , we solve the following minimization problem:

$$(u_i, \alpha_i) = \underset{\substack{u_i \in \mathcal{K}_A \\ 0 \leq \alpha_{i-1} \leq \alpha \leq 1}}{\operatorname{argmin}} \mathcal{E}_{t_i, \epsilon}(u, \alpha), \tag{16}$$

where $\mathcal{K}_A(t_i)$ denotes the set of kinematically admissible displacements and ϵ is some arbitrarily small parameter.

2.5. Link with gradient damage models

We have introduced our regularized energy (12) as a “phase-field” numerical approximation of a “sharp interface problem” (1). In the last few years, there has been a growing trend in studying a broad class of *rate independent gradient damage models*, to which (12) belongs. In this setting, the field α is seen as an internal damage variable, and ϵ as a material’s internal length [29,37,30,17]. The governing principle for the rate independent evolution is then similar to that of Definition 1, where the irreversibility condition becomes the growth of the damage variable, and unilateral global minimality is replaced by unilateral stability with respect to admissible changes of the damage variable and displacement field. There are growing evidences that both views coincide when the size of the internal length is small compared to the domain size, and in regimes where stability in the sense of Griffith is achieved. In this article, we do not try to investigate the sometimes subtle role of the regularization parameter, but focus on qualitative comparison of crack path, when these models are seen as an approximation of Francfort and Marigo’s variational model of fracture.

3. Numerical implementation

Our minimization strategy for (12) is now classical [13]. At each time step, it is achieved by alternating minimizations with respect to u and α until convergence, leveraging the separate convexity of the regularized energy with respect to each field.

In this algorithm, the spatial discretization is done using the Galerkin finite element method. The first step to obtain u is a simple convex problem implemented by solving the associated Euler–Lagrange equation (*i.e.*, an elasticity problem). In the second step to solve for α we use a bounded reduced space Newton minimization scheme for the discrete energy [38]. The variational approach to fracture mechanics requires spatial resolution of discretization to be at most of the order of the characteristic approximation length ϵ . The resulting problems are often very large and

necessitate the use of a parallel programming paradigm and the complex numerical tools therein. Our implementation relies on the distributed data structures provided by `libMesh` [39] and for linear algebra on `PETSc` [40,41].

3.1. Backtracking schemes

Like many other gradient based minimizations schemes, when dealing with a nonlinear set of equations, the alternate minimization cannot be guaranteed to converge to a global minimum of (12) but is known to converge to a stationary point of the total energy [42]. The foundation of the backtracking algorithm proposed and discussed in depth in [13] is to derive an additional necessary condition for optimality of a time evolution, and a algorithmic way to ensure that it is satisfied.

Consider a monotonically increasing loading and two loading steps t_i and t_j such that $t_j \leq t_i$. If the pair (u_i, α_i) is admissible for (12) at time $t = t_i$, then the pair $(\frac{t_j}{t_i}u_i, \alpha_i)$ is admissible for time $t = t_j$. Therefore, if the pair (u_j, α_j) is the global minimizer at time $t = t_j$, then $\mathcal{E}_{t,\epsilon}(u_j, \alpha_j) \leq \mathcal{E}_{t,\epsilon}(\frac{t_j}{t_i}u_i, \alpha_i)$, so that for any $0 \leq i \leq N$, we have

$$\mathcal{E}_{t,\epsilon}(u_j, \alpha_j) \leq \left(\frac{t_j}{t_i}\right)^2 \mathcal{P}_{t,\epsilon}(u_i, \alpha_i) + \mathcal{S}_\epsilon(\alpha_i), \quad \forall 0 \leq j \leq i. \quad (17)$$

In the Backtracking algorithm, condition (17) is checked against all previously computed time steps upon convergence of the alternating minimization algorithm. If a violation is detected *i.e.*, if an admissible pair attaining a lower energy for a past step has been constructed, the time evolution backtracks to that step using the current configuration as an initial guess.

Algorithm 1 the backtracking algorithm.

```

1: Set  $\alpha_0 = 0$ .
2: Let  $\delta_{BT} > 0$ ,  $\delta_{altmin}$  be given tolerance parameters.
3: for  $n = 0$  to  $N$  do
4:    $\alpha_i^0 \leftarrow \alpha_{n-1}$ 
5:   while  $|\alpha^j - \alpha^{j-1}|_{L^\infty} \geq \delta_{altmin}$  do
6:      $u^{j+1} \leftarrow \underset{u \in \mathcal{K}_A}{\operatorname{argmin}} E_\epsilon(u, \alpha^j)$ 
7:      $\alpha^{j+1} \leftarrow \underset{\alpha_i \leq \alpha \leq 1}{\operatorname{argmin}} E_\epsilon(u^{j+1}, \alpha)$ 
8:      $j \leftarrow j + 1$ 
9:    $u_n \leftarrow u^j$ 
10:   $\alpha_n \leftarrow \alpha^j$ 
11:   $\mathcal{P}_n \leftarrow \mathcal{P}_t(u_n, \alpha_n)$ 
12:   $\mathcal{S}_n \leftarrow \mathcal{S}_t(u_n, \alpha_n)$ 
13:  for  $k = 1 \dots n - 1$  do
14:    if  $\mathcal{P}_k + \mathcal{S}_k - \left(\frac{t_k}{t_n}\right)^2 \mathcal{P}_n - \mathcal{S}_n \geq \delta_{BT}$  then
15:       $\alpha^0 \leftarrow \alpha_n$ 
16:       $n \leftarrow k$ 
17:    goto 5.

```

The backtracking search loop (steps 13–17 of Algorithm 1) is only performed upon convergence of the alternating minimizations algorithm. The first modification we propose is to perform it after *each* alternate minimization step, in order to better explore the configuration space (u, α) .

Of course, checking the backtracking condition for every iteration of the alternate minimization against all the previous time steps may be computationally expensive. Additionally, remark that this loop can be performed for increasing or decreasing values of k . This is potentially interesting since different directions can explore different minima of the configuration space. This leads us to introducing a *deep backtracking* algorithm (Algorithm 2) based on three parameters describing how often and in which order condition (17) is checked.

1. the interval b_i controls how often the backtracking search loop is performed;
2. the direction $b_d = \pm 1$ sets which of “older” or “newer” steps are checked first;
3. the scope b_s controls the interval in which the backtracking search loop is performed.

Algorithm 2 the deep backtracking algorithm.

```

1: Set  $\alpha_0 = 1$ .
2: Let  $\delta_{BT} > 0$ ,  $\delta_{altmin}$  be given tolerance parameters.
3: for  $n = 0$  to  $N$  do
4:   if  $n > n_{\max}$  then
5:      $n_{\max} \leftarrow n$ 
6:    $\alpha_i^0 \leftarrow \alpha_{n-1}$ 
7:   while  $|\alpha^j - \alpha^{j-1}|_{L^\infty} > \delta_{altmin}$  do
8:      $u^{j+1} \leftarrow \operatorname{argmin}_{u \in \mathcal{K}_A} E_\epsilon(u, \alpha^j)$ 
9:      $\alpha^{j+1} \leftarrow \operatorname{argmin}_{\alpha_i \leq \alpha \leq 1} E_\epsilon(u^{j+1}, \alpha)$ 
10:    if  $j \bmod b_i = 0$  then
11:       $\mathcal{P}_n^j \leftarrow \mathcal{P}_t(u^j, \alpha^j)$ 
12:       $\mathcal{S}_n^j \leftarrow \mathcal{S}_t(u^j, \alpha^j)$ 
13:      if  $b_d = 1$  then
14:         $k_0 = \max((n_{\max} - b_s), 1)$ 
15:         $k_1 = n - 1$ 
16:      else
17:         $k_0 = n - 1$ 
18:         $k_1 = \max((n_{\max} - b_s), 1)$ 
19:      for  $k = k_0$  to  $k_1$  do
20:        if  $\mathcal{P}_k + \mathcal{S}_k - \left(\frac{t_k}{t_n}\right)^2 \mathcal{P}_n^j - \mathcal{S}_n^j \geq \delta$  then
21:           $\alpha^0 \leftarrow \alpha^j$ 
22:           $n \leftarrow k$ 
23:          goto 7.
24:       $j \leftarrow j + 1$ 
25:     $u_n \leftarrow u^{j+1}$ 
26:     $\alpha_n \leftarrow \alpha^{j+1}$ 

```

In the next sections, we illustrate the influence of each parameter and how they can be tuned to match well known experimental results.

4. Numerical experiments

4.1. The L-shaped plate

The L-shaped experiment reported in [43] and described in Fig. 1 is a popular setting for the validation of numerical techniques [44–46,9]. The experiments are done using a concrete L-shape panel 10 cm in width fixed to a mortar foundation at the bottom and loaded by a hydraulic system connected to a mortar jacket on its right side. The material properties taken from the aforementioned references are listed in Table 1.

For this problem, we performed series of computations using backtracking or deep backtracking, and varying the interval, scope, and direction for two different mesh sizes. The sample geometry and loadings are depicted in Fig. 1. In order to avoid changes in “effective toughness” induced by the relative magnitude of the mesh size h and regularization parameter ϵ as discussed in [13], we kept their ratio fixed $h/\epsilon = 5$. In order to speed up computations, we also used a coarser mesh and forced $\alpha = 0$ in the areas represented in gray in the schematics, while setting $\alpha = 1$ along the corner

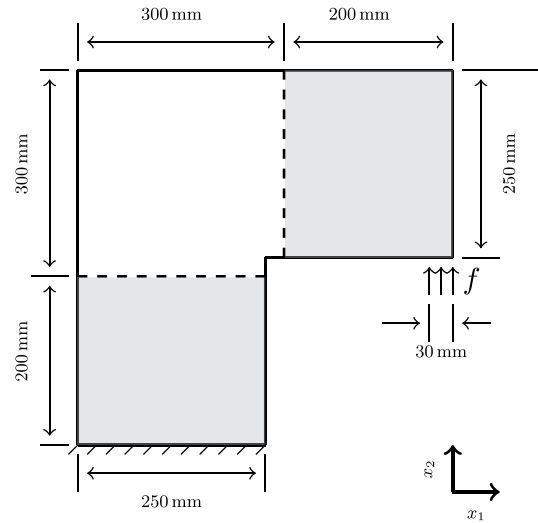


Fig. 1. Schematics of the L-shaped plate experiment from [43], $\alpha \equiv 0$ in gray areas.

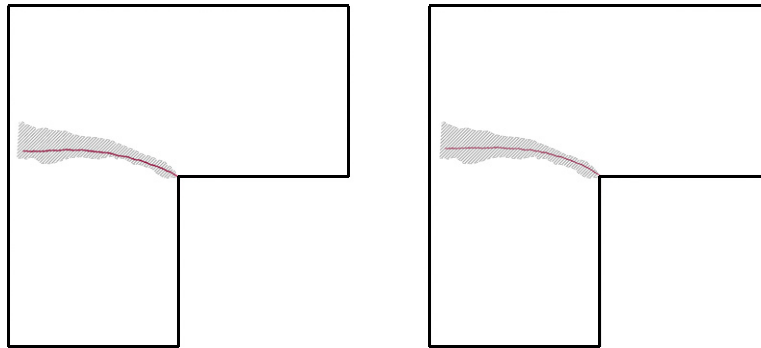


Fig. 2. Crack path in the L-shaped plate: comparison of the numerical simulations results with experimental data (in gray) from [43]. Crack path ($0.9 \leq \alpha \leq 1$ in red) for the characteristic approximation length (left) $h = 0.3125$ mm and $\epsilon = 1.5625$ mm. (For interpretation of the references to color in this figure legend, the reader is referred to the web version of this article.)

Table 1
Material properties for the L-shape plate [43].

E (GPa)	ν	G_c (N m ⁻¹)
25.85	0.18	95

where crack nucleation was expected. In all cases, we observed an elastic phase, followed by the sudden nucleation of a short crack originating from the corner of the domain and subsequently propagating in a stable manner.

As expected, we observed that the crack path is not affected by the choice of the backtracking algorithm. Fig. 2 shows the final crack path for two different values of the regularization parameter ϵ . In both cases, the computed crack path falls within the range of experimental observations from [43], but the initial crack angle exhibits some sensitivity upon the value of ϵ .

A closer look at crack nucleation highlights how the backtracking algorithm has little influence on the crack angle and length at activation, as demonstrated by Fig. 3 and Table 2 showing the crack geometry and critical activation load for the standard and deep backtracking algorithm, and two values of ϵ . As expected, the standard backtracking leads to lower critical load at nucleation (see Table 2). Deep backtracking with a forward direction, an interval $b_i = 1$ and a scope $b_s = \infty$ leads to a shorter crack, and an even lower critical load, which is consistent with the fact that this algorithm is more exploratory than the original one.

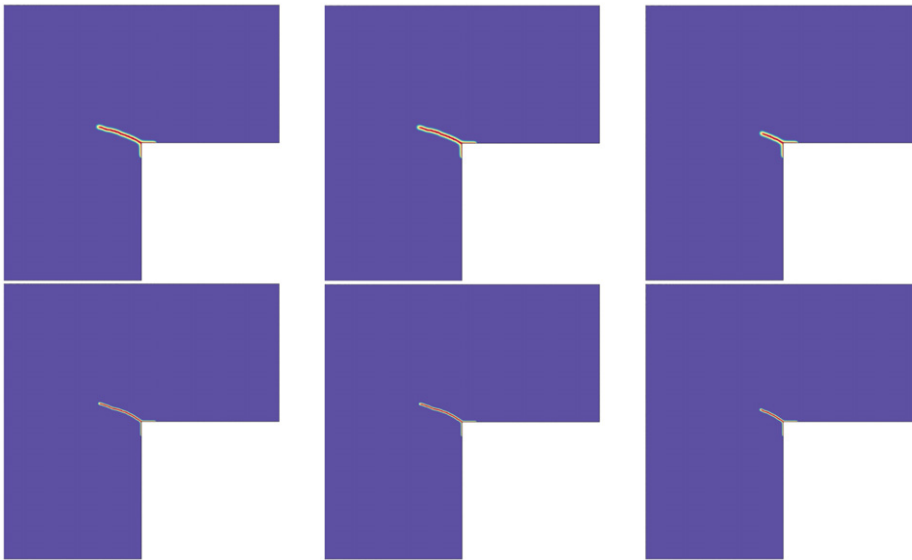


Fig. 3. Pseudo-color plot of the regularized crack field α after nucleation of a crack for the L-shaped plate without backtracking (left), with the original backtracking (center) or the proposed deep backtracking (right). The material properties are that of Table 1. The mesh size and regularization length are $h = 0.625$ mm, $\epsilon = 3.125$ mm (top row) and $h = 0.3125$ mm, $\epsilon = 1.5625$ mm.

Table 2
L-shaped plate numerical simulation results for different backtracking algorithms.

ϵ (mm)	Backtracking algorithm	Critical vertical displacement (mm)	Critical load (kN)	Initial crack length (mm)	Initial crack angle
3.125	None	0.2496	14.6788	87.95	26.06°
3.125	Original	0.2352	13.9066	87.95	26.06°
3.125	Deep	0.2304	13.6322	43.39	26.06°
1.5625	None	0.2624	15.6654	96.26	33.21°
1.5625	Original	0.2448	14.6482	96.26	33.21°
1.5625	Deep	0.2416	14.4592	52.81	33.21°

In all cases, the crack angle falls within the rather large bracket of experimental measurements of 0° – 43° , but the critical load is overestimated, and its value appears to depend strongly on the value of ϵ . This effect is clearly visible from the force–displacement diagrams in Fig. 4. This is again consistent with the finding of [29] who suggest that the link between a material’s yield stress and regularization length at the onset of loss of stability of the elastic solution in uniaxial tension experiment can be used to calibrate the regularization parameter. Using a critical yield stress of 2.7 MPa from [45] and following the approach of [17] leads to an internal length $\epsilon = 126.32$ mm, which is within the range of accepted values for concrete. Fig. 5 shows the force–displacement diagram and the damage field at the onset of crack nucleation, and after full evolution. The good match between measured and computed force–displacement diagrams before nucleation and for short cracks give credit to this approach. However, for such a large value of ϵ , the damage distribution is very diffuse, rendering the interpretation of this experiment within the brittle fracture realm dubious. If the widely accepted order of magnitude of 10–100 mm for the internal length of concrete is to be trusted, this experiments needs to be conducted on a much larger sample in order to be used for the validation of brittle fracture numerical simulations.

One of the features of the variational approach to fracture is the effortless generalization to the three dimensions. Fig. 6 shows a 3-D (isovolume) rendering of smeared fracture field $0.9 \leq \alpha \leq 1$ which was done using approximately 187,000 linear tetrahedral elements with average edge size $h_f = 2.5$ mm in the brittle computational domain (look at Fig. 1) and regularization length $\epsilon = 5$ mm. Again, the crack path falls with the envelope of experimentally observed paths, demonstrating the ability of our approach to correctly identify crack path on three dimensions.

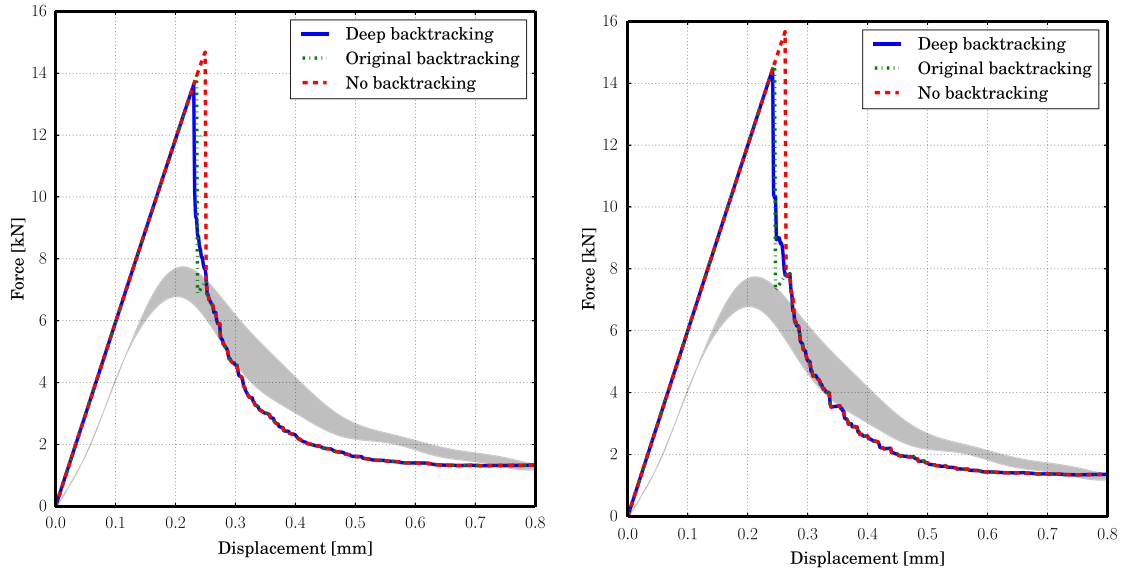


Fig. 4. Applied force as a function of the vertical displacement at the lower left corner of the plate: comparison of the numerical simulations results with the experimental data (in gray) [43] crack path ($0.9 \leq \alpha \leq 1$ in red) for the characteristic approximation length (left) $\epsilon = 3.125$ mm (right) $\epsilon = 1.5625$ mm. (For interpretation of the references to color in this figure legend, the reader is referred to the web version of this article.)

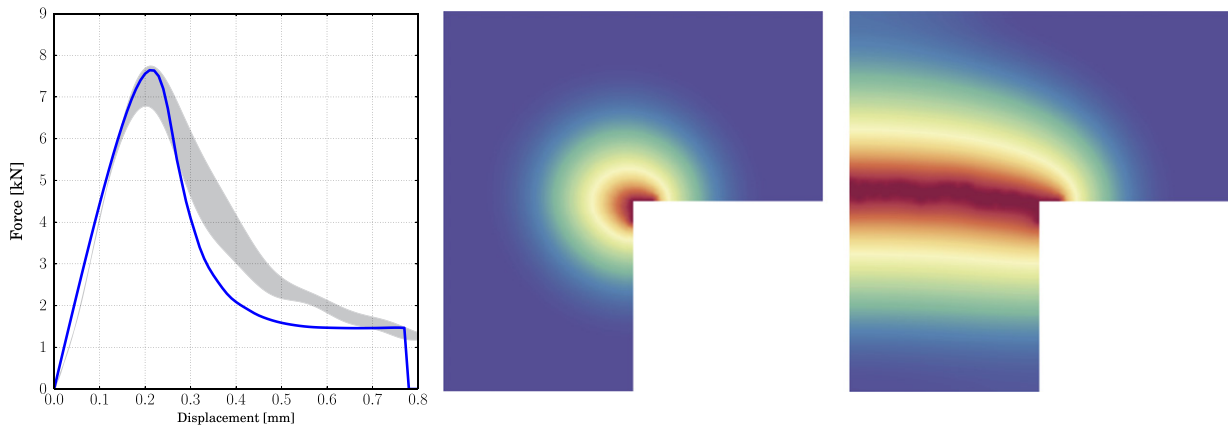


Fig. 5. Force–displacement curve, damage at the critical load and upon final crack evolution for the L-shaped domain with an internal length derived from the material’s yield stress, and showing large diffuse damage.

4.2. A three-point bending experiments

In order to highlight the differences between standard and deep backtracking, we turn our attention an asymmetrically notched three-point bending experiment on Plexiglas sheets originally described in [47]. The experiment was designed so that small variations of the sample geometry and loading would lead to large changes in crack path, and is therefore a good test when estimating a method’s ability to identify crack path [48–51]. The sample geometry and its loading are shown in Fig. 7, the material properties in Table 3, and the location and length of the initial crack in two different configurations in specific values of the location of the top, middle and bottom holes (indicated respectively by T, M, and B) in Table 4.

In order to reduce the computational cost and eliminate the need to deal with potential compressive cracks around the support and force application points, we used a coarse mesh and forced $\alpha = 0$ in the area shown in gray in Fig. 7. The central part of the domain was meshed with linear triangular finite element with an average edge length of average 0.01 in. (.254 mm), for a total of approximately 1.35 million elements.

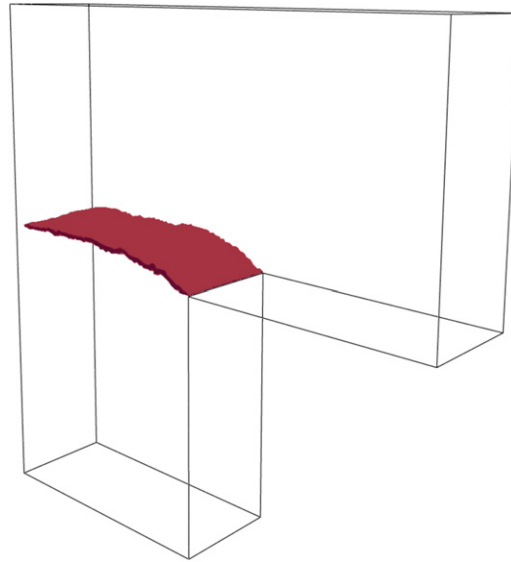


Fig. 6. Crack path in a three-dimensional L-shaped numerical simulation.

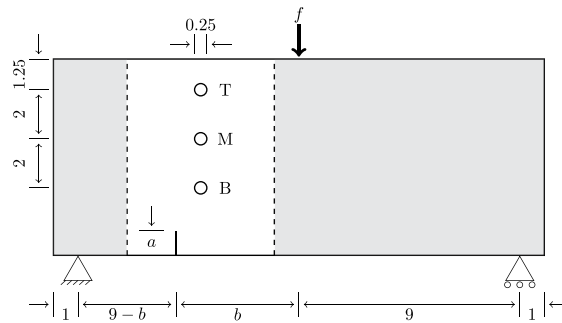


Fig. 7. Three-point bending experiment schematics, $\alpha \equiv 0$ in gray areas (all the sizes are in inches).

Table 3
Material properties for the asymmetric three-point bending.

E	ν	G_c
450 kpsi (3.102 GPa)	0.35	1.73 lbf/in. (304.321 N m ⁻¹)

Table 4
Geometry of the asymmetric three-point bending sample.

Configuration	I	II
a	1 in (25.4 mm)	2.5 in. (63.5 mm)
b	6 in (152.4 mm)	6 in. (152.4 mm)

Fig. 8 shows a comparison between the computed crack path for configuration I (see Table 4) and experimental results. Without backtracking, we observe that after a long elastic phase, a long crack suddenly forms, spanning from the initial notch to the middle hole, then the upper hole, then continuing through the domain itself (see Fig. 8-left). The computed crack path only matches experimental data until it reaches the vicinity of the middle hole, and significantly deviates afterwards. As described in [15,13], in such situation there is no expectation that energy balance (17) should be satisfied, and indeed, it is not. Using the original backtracking algorithm leads to an evolution following the

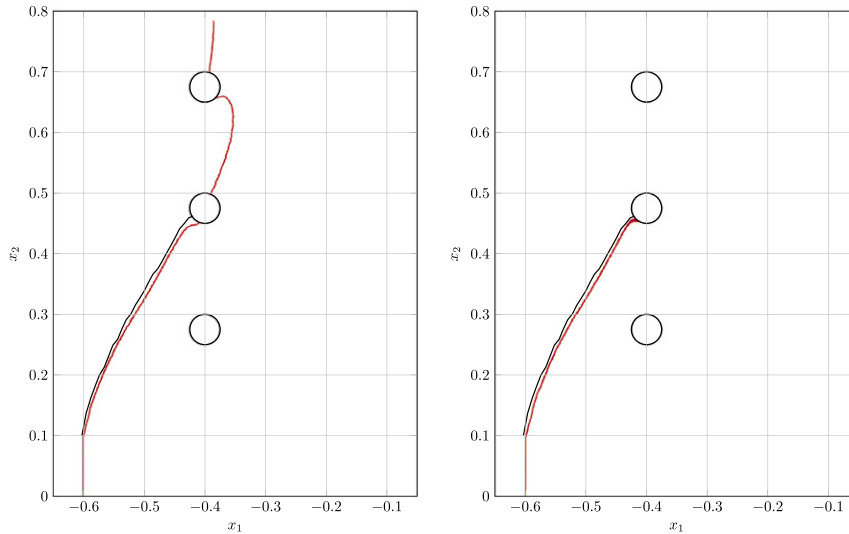


Fig. 8. Asymmetric three-point bending experiment configuration **I**: comparison of crack path ($0.9 \leq \alpha \leq 1$ in red) with experimental data [43] (left) original backtracking (right) deep backtracking.

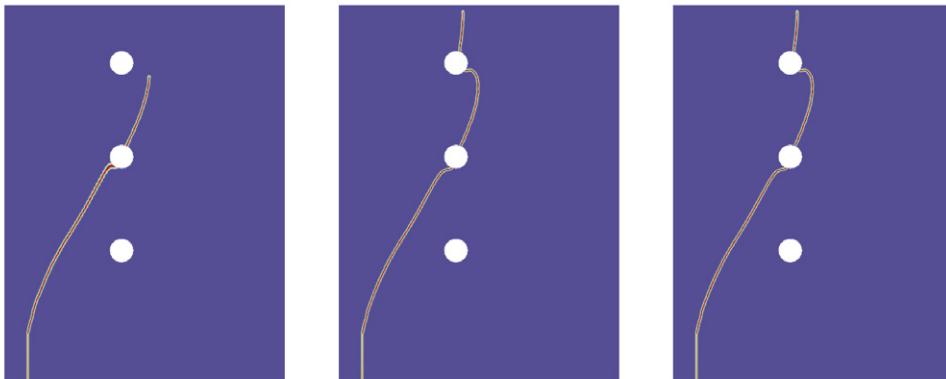


Fig. 9. Asymmetric three-point bending experiment smeared fracture field α at nucleation for configuration **I** using (left) deep backtracking (middle) original backtracking (right) no backtracking.

same path (recall that the backtracking search loop is only performed after the alternate minimizations algorithm has converged, *i.e.*, once the crack path from Fig. 8-left has been identified), but a crack growing at a significantly lower loading, so that total energy balance is satisfied. Using the deep backtracking, still leads to sudden crack propagation (see Fig. 9), but along a path that is closer to that observed in experiments, and does not restart from the middle hole. The crack path is shown for a computation with $b_i = 5$, $b_s = \infty$ and $b_d = +1$ is shown in Fig. 8-right. We performed multiple experiments varying the value of the three backtracking parameters and obtained similar results, as long as the interval is not set “too high” (indeed, $b_i = \infty$ would correspond to the original backtracking). Additionally, we observed that the deep backtracking leads to a solution energetically favorable compared to the original one (see Fig. 12). This is expected as the deep backtracking algorithm explores a larger portion of the configuration space. Of course, we do not claim that the computed solution is a global energy minimizer.

A second set of numerical simulations for configuration **II** highlights a similar behavior of the deep compared to standard backtracking. Both the solution without and with standard backtracking lead to a sudden crack propagation through the middle hole, ending in the bulk of the domain whereas the deep backtracking consistently leads to a crack reaching the top hole, as in the experiments, despite being deflected by the presence of the middle hole (see Figs. 10 and 11). Again, the deep backtracking algorithm leads to a energetically favorable solution over standard

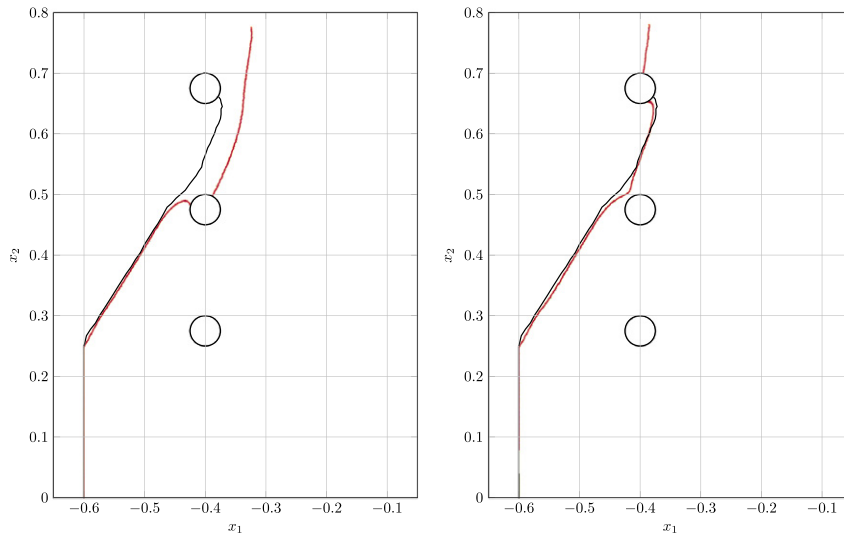


Fig. 10. Asymmetric three-point bending experiment configuration II: comparison of crack path ($0.9 \leq \alpha \leq 1$ in red) with experimental data [43] (left) original backtracking (right) deep backtracking. (For interpretation of the references to color in this figure legend, the reader is referred to the web version of this article.)

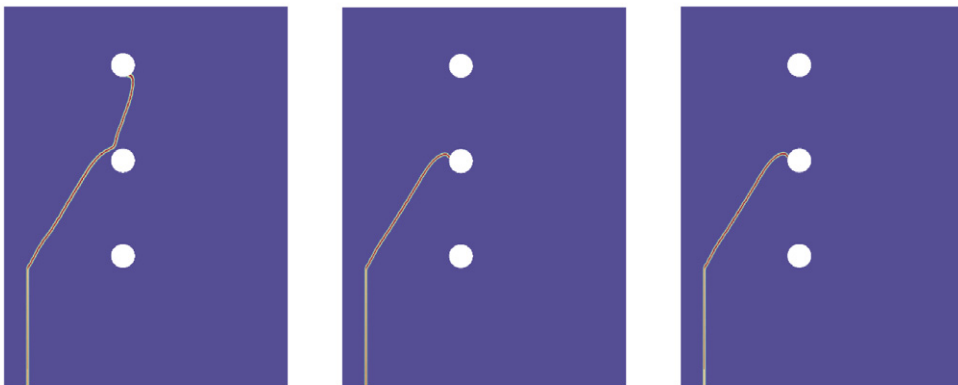


Fig. 11. Asymmetric three-point bending experiment smeared fracture field α at nucleation for configuration II using (left) deep backtracking (middle) original backtracking (right) no backtracking.

backtracking. We note a significant difference between the numerical and experimental solution as our numerical simulation consistently lead to a crack reactivating out of the top hole, at its onset.

Again, no significant difference in the primary crack path (from the notch to the first intersection with one of the holes) was observed when the numerical simulations performed were done using different combination of the auxiliary deep backtracking parameters (*i.e.*, direction, scope, interval).

4.3. The Nooru-Mohamed tension shear experiments

In the Nooru-Mohamed tension shear experiment, the double-edge-notched specimen is subject to mixed tensile and shear loads [52]. The result of this experiments has been used for validation purposes in number of articles [53–56]. Fig. 13 shows the schematic of the test specimen and Table 5 summarizes the material properties used in the numerical simulations. Here the loading protocol 4b, as defined in [52] was investigated numerically. This protocol specifies the loading path as follows: (i) apply constant shear load f_s while keeping $f_n \equiv 0$, (ii) apply monotonically increasing f_n while keeping f_s constant. In the experiments, proper care was taken to ensure that the direction of the two loads always remained perpendicular; to achieve the same results in the simulation, the elastic step of alternate minimization was obtained by superposition of three loadings as depicted in Fig. 14.

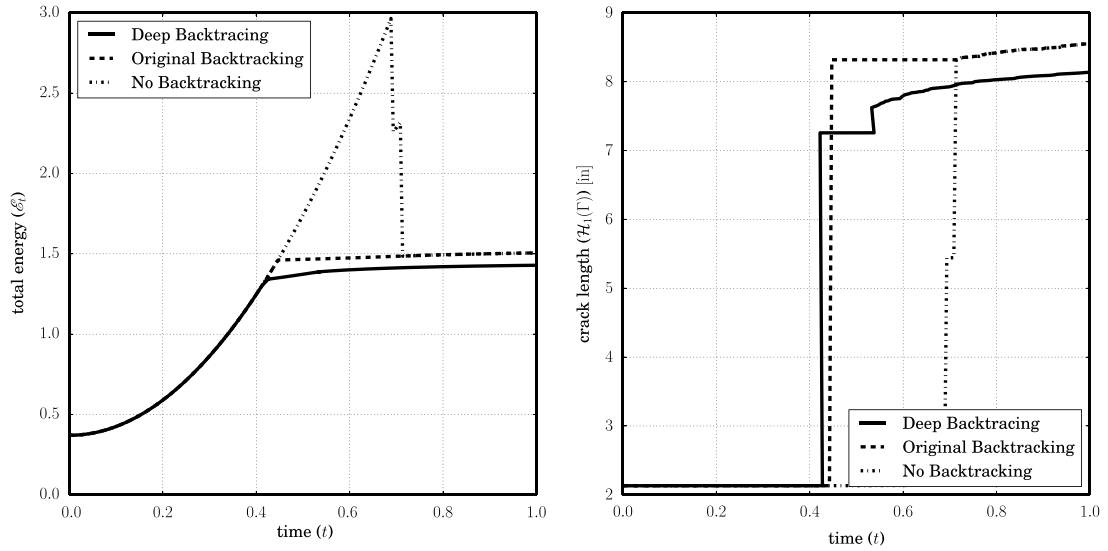


Fig. 12. Asymmetric three-point bending experiment configuration II: comparison of total energy (left) and crack length (right) using different backtracking algorithms.

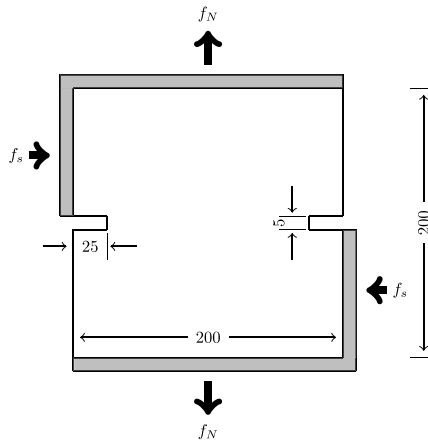


Fig. 13. Tension shear experiment schematics (all the sizes are in mm, gray areas are rigid).

Table 5
Material properties for tension shear experiment.

E (GPa)	ν	G_c (N m ⁻¹)
30	0.2	110

Both backtracking algorithms can be extended to account for this loading by subtracting the work of constant loads from the bulk elastic energy so that the backtracking condition (line 14 in Algorithm 1 or line 20 in Algorithm 2) becomes

$$\mathcal{P}_k + \mathcal{I}_k + \mathcal{B}_k - \left(\frac{t_k}{t_n}\right)^2 \mathcal{P}_n^j - \mathcal{I}_n^j - \mathcal{B}_n^j \geq \delta, \tag{18}$$

where \mathcal{B} is the bulk energy due to constant loads (first and second loading stages in Fig. 14).

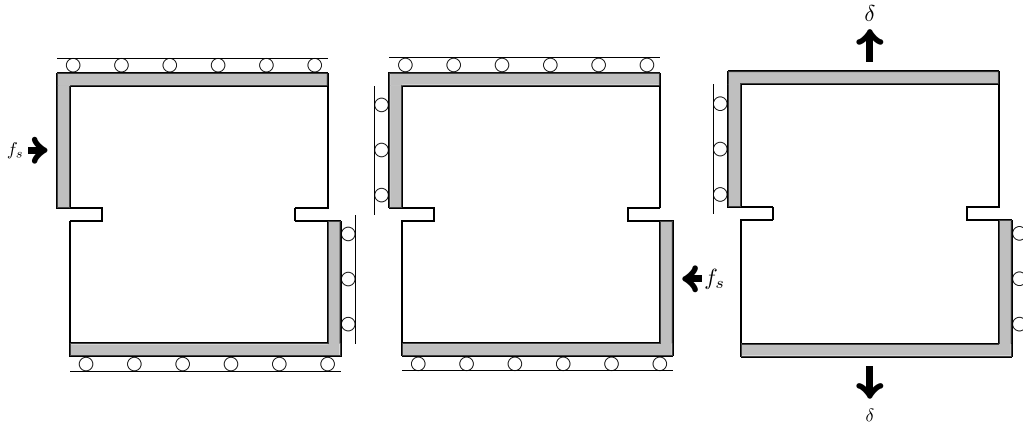


Fig. 14. Elastic substeps for the tension shear numerical simulations.

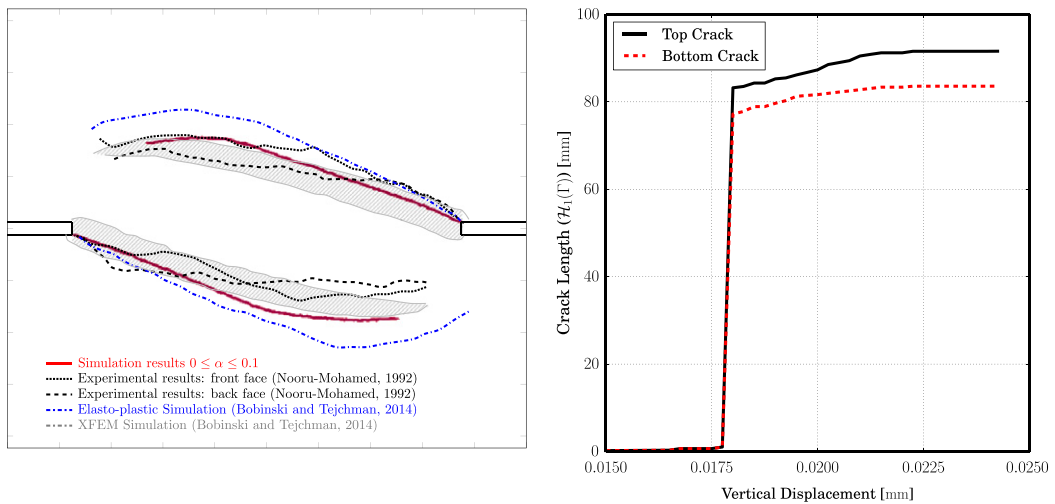


Fig. 15. Nooru-Mohamed experiment: (left) comparison of simulated crack path ($0.9 \leq \alpha \leq 1$ in red) with experimental data [52] front face (dotted black line), back face (dashed black line), elasto-plastic simulation (gray hashed area) [57], and XFEM simulation (blue dash-dotted line) [57]. (right) Crack length as a function of the vertical displacement top crack in black and bottom crack in red. (For interpretation of the references to color in this figure legend, the reader is referred to the web version of this article.)

The loading protocol highlighted above results in the rotation of principal stresses as the crack propagates which, in turn, results in two curvilinear crack paths. The computations in this section were done using approximately 337,000 linear triangular elements with an average 0.5 mm side length (see Fig. 7).

In this computation, we observed an elastic phase followed by the nucleation of two cracks of non-zero length, which then propagate progressively. The type of backtracking algorithm did not change the qualitative behavior or the overall path, but again altered the critical load upon which the crack propagated, with as expected an earliest onset for the standard backtracking then deep backtracking.

Fig. 15 shows a comparison between the numerical results and the experimental data for $f_s = 10$ kN along with simulations based on XFEM and an elasto-plastic model [57]. In the variational approach, crack evolution is governed by a *global* principle (energy minimization) instead of a *local one* (criticality of the elastic energy release rate at each crack tip). Owing to the lack of uniqueness of solution, it may happen that symmetric sets of asymmetric solutions be energy minimizers. Here, we observed that the overall path nearly symmetric and that both cracks are nucleated simultaneously (see Fig. 16). However, there was a small difference in crack length at nucleation and throughout the evolution (see Fig. 15-(right)). It is not clear if this behavior illustrates the possible non-uniqueness often solution of the problem, or is a spurious effect induced by the lack of symmetry of the mesh or numerical error.

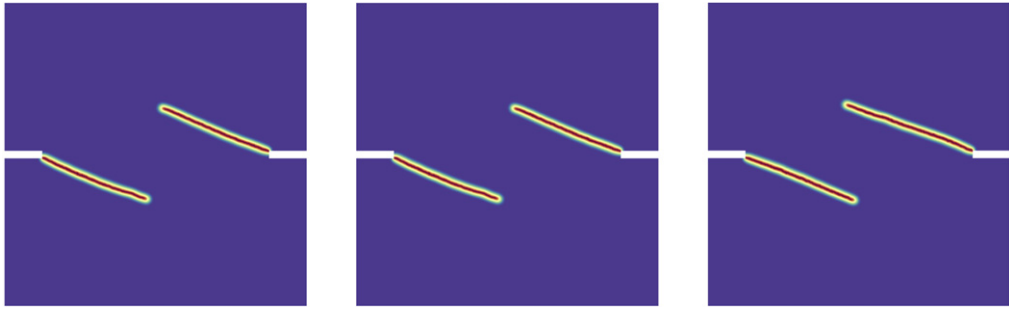


Fig. 16. Pseudo-color plot of the regularized crack field α after nucleation of a crack for the L-shaped plate without backtracking (left), with the original backtracking (center) or the proposed deep backtracking (right). The material properties are that of Table 5. The mesh size and regularization length are $h = 0.5$ mm, $\epsilon = 2.5$ mm.

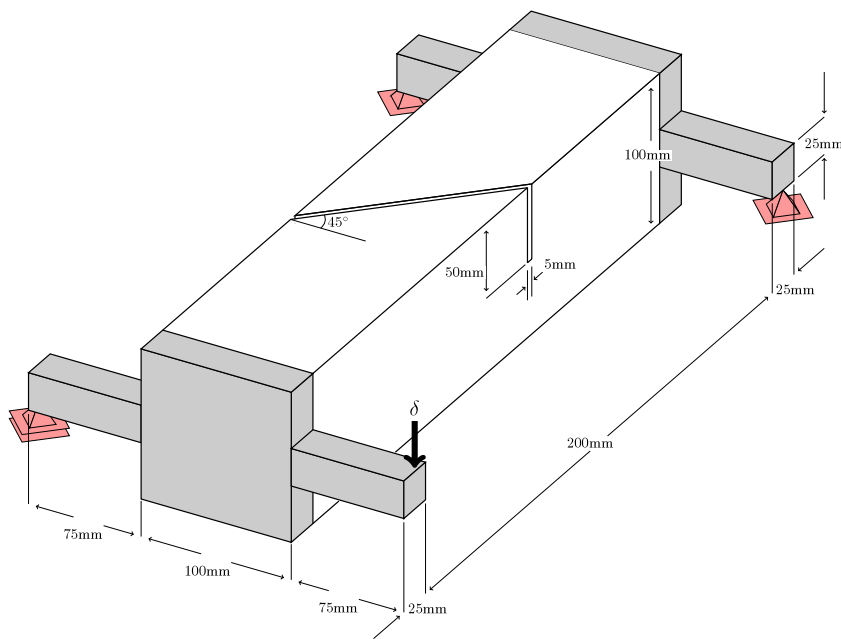


Fig. 17. Schematics of the Brokenshire torsion experiment with oblique crack.

Table 6
Material properties for Brokenshire torsion experiments.

E (GPa)	ν	G_c (N m ⁻¹)
35	0.2	110

4.4. The Brokenshire torsion experiments

We finally focused our attention on a fully three-dimensional problem initially presented in [58] and previously investigated in a number of articles [53,59–61]. The Brokenshire test consists of a specimen with a 45° oblique notch subject to a torsional load (see Fig. 17 for a schematic description of the domain geometry). In experiments, the frame (shown in gray in Fig. 17) is held at three of its end points, while the downward vertical displacement of the fourth one (facing the viewer in the figure) is prescribed. All the computations in this section were done using approximately 1.45 million linear tetrahedral elements with an average edge length of 2.5 mm near the oblique. The material properties used in our computations are consistent with the literature, and indicated in Table 6.

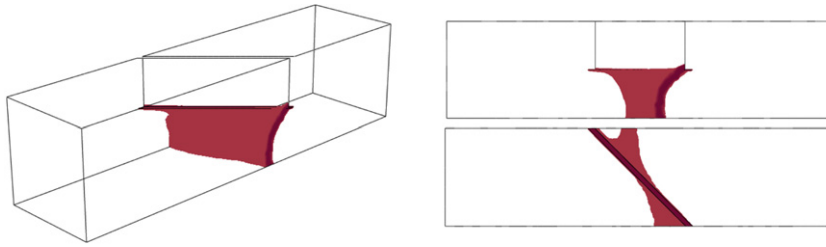


Fig. 18. Brokenshire torsion simulation ($\epsilon = 12.5$ mm): final crack geometry (left) isometric view (right top) front view (right bottom) top view.

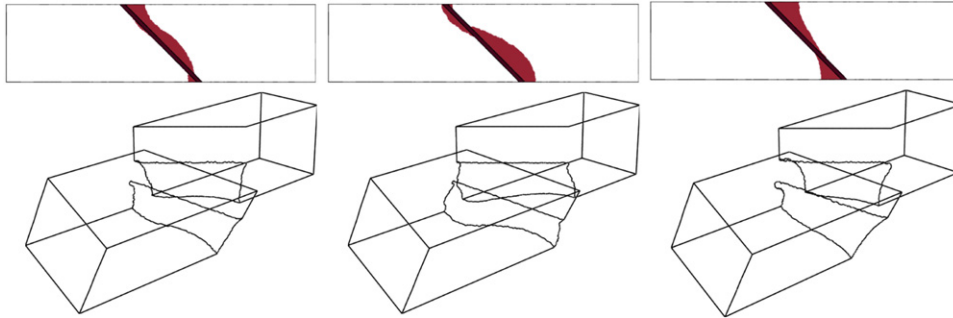


Fig. 19. Brokenshire torsion simulation: (top) Top view of the final fracture geometry $0.9 \leq \alpha \leq 1.0$, (bottom) Isometric view of the final deformed geometry: (left) $\epsilon = 2.5$ mm (middle) $\epsilon = 5$ mm (right) $\epsilon = 12.5$ mm.

For such a problem, quantitative comparison with experiments is difficult, but the qualitative behavior that we observed, a three dimensional crack front turning to accommodate for change in the maximum normal stresses' orientation as it propagate (see Fig. 18) is consistent with experiments. However, as previously noticed in the literature [53,59–61], we also observed that the crack path is very sensitive to small changes in geometry and loading, or to changes in the regularization parameter ϵ . Fig. 19 shows changes in the final fracture geometry (isovolume renderings of the fracture field $0.9 \leq \alpha \leq 1.0$) and the final deformed geometry for three different values of ϵ .

5. Conclusions

In this article, we performed several validation experiments for the variational approach to fracture [13], implemented through a regularized energy, focusing on situations where complex crack paths arise. We highlighted the adequacy of this approach for quantitative prediction of crack paths, without *a priori* hypotheses. We improved significantly on the backtracking algorithm by devising a variant exploring more states in configuration space.

In four distinct problems, we performed numerical simulations predicting crack paths that are consistent with experiments and the most accepted numerical literature. When nucleation of a crack with non-zero length is observed, the critical loading upon which cracks nucleate is shown to depends significantly on the regularization parameter ϵ of the regularized energy. This phenomenon should highlight the importance of the extensive study of gradient damage models in the one-dimensional case [30], and how it can be leveraged in numerical simulations, as in [17].

Acknowledgments

AM and BB's work was supported in part by the National Science Foundation grant DMS-1312739. Some numerical experiments were performed using resources of the Extreme Science and Engineering Discovery Environment (XSEDE), which is supported by National Science Foundation grant number OCI-1053575 under the Resource Allocation TG-DMS060014.

References

- [1] M. Ortiz, A. Pandolfi, Finite-deformation irreversible cohesive elements for three-dimensional crack-propagation analysis, *Int. J. Numer. Methods Engrg.* 44 (1999) 1267–1282.
- [2] X.P. Xu, A. Needleman, Numerical simulations of fast crack-growth in brittle solids, *Internat. J. Solids Struct.* 42 (9) (1994) 1397–1434.

- [3] P. Areias, T. Belytschko, Analysis of three-dimensional crack initiation and propagation using the extended finite element method, *Int. J. Numer. Methods Eng.* 63 (5) (2005) 760–788.
- [4] N.M.O. Mões, J. Dolbow, T. Belytschko, A finite element method for crack growth without remeshing, *Int. J. Numer. Methods Engrg.* 46 (1999) 131–150.
- [5] A. Karma, A.E. Lobkovsky, Unsteady crack motion and branching in a phase-field model of brittle fracture, *Phys. Rev. Lett.* 92 (24) (2004) 245–510.
- [6] C. Miehe, F. Welschinger, M. Hofacker, Thermodynamically consistent phase-field models of fracture: Variational principles and multi-field FE implementations, *Int. J. Numer. Methods Engrg.* 83 (10) (2010) 1273–1311.
- [7] C. Miehe, M. Hofacker, F. Welschinger, A phase field model for rate-independent crack propagation: Robust algorithmic implementation based on operator splits, *Comput. Methods Appl. Mech. Engrg.* 199 (45–48) (2010) 2765–2778.
- [8] G. Allaire, F. Jouve, N. Van Goethem, Damage and fracture evolution in brittle materials by shape optimization methods, *J. Comput. Phys.* 230 (12) (2011) 5010–5044.
- [9] P.E. Bernard, N. Moës, N. Chevaugeon, Damage growth modeling using the thick level set (TLS) approach: Efficient discretization for quasi-static loadings, *Comput. Methods Appl. Mech. Engrg.* 233 (2012) 11–27.
- [10] B. Schmidt, F. Fraternali, M. Ortiz, Eigenfracture: An eigendeformation approach to variational fracture, *Multiscale Model. Simul.* 7 (3) (2009) 1237–1266.
- [11] G.A. Francfort, J.-J. Marigo, Revisiting brittle fracture as an energy minimization problem, *J. Mech. Phys. Solids* 46 (8) (1998) 1319–1342.
- [12] B. Bourdin, G.A. Francfort, J.-J. Marigo, Numerical experiments in revisited brittle fracture, *J. Mech. Phys. Solids* 48 (4) (2000) 797–826.
- [13] B. Bourdin, G.A. Francfort, J.-J. Marigo, The variational approach to fracture, *J. Elasticity* 91 (1) (2008) 5–148.
- [14] B. Bourdin, The variational formulation of brittle fracture: numerical implementation and extensions, in: *IUTAM Symposium on Discretization Methods for Evolving Discontinuities*, Springer, 2007, pp. 381–393.
- [15] B. Bourdin, Numerical implementation of the variational formulation for quasi-static brittle fracture, *Interfaces Free Bound.* 9 (3) (2007) 411–430.
- [16] C. Maurini, B. Bourdin, G. Gauthier, V. Lazarus, Crack patterns obtained by unidirectional drying of a colloidal suspension in a capillary tube: experiments and numerical simulations using a two-dimensional variational approach, *Internat. J. Fracture* 184 (1–2) (2013) 75–91.
- [17] B. Bourdin, J.-J. Marigo, C. Maurini, P. Sicsic, Morphogenesis and propagation of complex cracks induced by thermal shocks, *Phys. Rev. Lett.* 112 (1) (2014) 014301.
- [18] A.A. Léon Baldelli, B. Bourdin, J.-J. Marigo, C. Maurini, Fracture and debonding of a thin film on a stiff substrate: analytical and numerical solutions of a 1d variational model, *Continuum Mech. Thermodyn.* 25 (2–4) (2013) 243–268.
- [19] A.A. Léon Baldelli, J.-F. Babadjian, B. Bourdin, D. Henao, C. Maurini, A variational model for fracture and debonding of thin films under in-plane loadings, *J. Mech. Phys. Solids* 70 (0) (2014) 320–348.
- [20] A. Mesgarnejad, B. Bourdin, M.M. Khonsari, A variational approach to the fracture of brittle thin films subject to out-of-plane loading, *J. Mech. Phys. Solids* 61 (11) (2013) 2360–2379.
- [21] F. Amiri, D. Millán, Y. Shen, T. Rabczuk, M. Arroyo, Phase-field modeling of fracture in linear thin shells, *Theor. Appl. Fract. Mech.* 69 (0) (2014) 102–109.
- [22] A. Abdollahi, I. Arias, Phase-field modeling of the coupled microstructure and fracture evolution in ferroelectric single crystals, *Acta Mater.* 59 (12) (2011) 4733–4746.
- [23] A. Abdollahi, I. Arias, Phase-field modeling of crack propagation in piezoelectric and ferroelectric materials with different electromechanical crack conditions, *J. Mech. Phys. Solids* 60 (12) (2012) 2100–2126.
- [24] C.J. Larsen, C. Ortner, E. Süli, Existence of solutions to a regularized model of dynamic fracture, *Math. Models Methods Appl. Sci.* 20 (7) (2010) 1021–1048.
- [25] B. Bourdin, C.J. Larsen, C.L. Richardson, A time-discrete model for dynamic fracture based on crack regularization, *Int. J. Fracture* 168 (2) (2011) 133–143.
- [26] M.J. Borden, C.V. Verhoosel, M.A. Scott, T.J.R. Hughes, C.M. Landis, A phase-field description of dynamic brittle fracture, *Comput. Methods Appl. Mech. Engrg.* 217–220 (0) (2012) 77–95.
- [27] A. Schlüter, A. Willenbücher, C. Kuhn, R. Müller, Phase field approximation of dynamic brittle fracture, *Comput. Mech.* (2014) 1–21.
- [28] A. Braides, Approximation of free-discontinuity problems, in: *Lecture Notes in Mathematics*, Springer-Verlag, 1998.
- [29] K. Pham, H. Amor, J.-J. Marigo, C. Maurini, Gradient damage models and their use to approximate brittle fracture, *Int. J. Damage Mech.* 20 (4) (2011) 618–652.
- [30] K. Pham, J.-J. Marigo, C. Maurini, The issues of the uniqueness and the stability of the homogeneous response in uniaxial tests with gradient damage models, *J. Mech. Phys. Solids* 59 (6) (2011) 1163–1190.
- [31] L. Ambrosio, V.M. Tortorelli, Approximation of functionals depending on jumps by elliptic functionals via Γ -convergence, *Communications on Pure Appl. Math.* 43 (8) (1990) 999–1036.
- [32] L. Ambrosio, V.M. Tortorelli, On the approximation of free discontinuity problems, *Boll. dell’Unione Mat. Italiana* 6 (1992) 105–123.
- [33] A. Chambolle, An approximation result for special functions with bounded variations, *J. Math. Pures Appl.* 83 (2004) 929–954.
- [34] A. Chambolle, Addendum to “an approximation result for special functions with bounded deformation” [*J. math. pures appl.* (9) 83 (7) (2004) 929–954]: the n-dimensional case, *J. Math. Pures Appl.* 84 (2005) 137–145.
- [35] M. Focardi, On the variational approximation of free-discontinuity problems in the vectorial case, *Math. Models Methods Appl. Sci.* 11 (663–684) (2001).
- [36] A. Giacomini, Ambrosio-Tortorelli approximation of quasi-static evolution of brittle fractures, *Calc. Var. Partial Differential Equations* 22 (2) (2005) 129–172.
- [37] K. Pham, J.-J. Marigo, From the onset of damage to rupture: construction of responses with damage localization for a general class of gradient damage models, *Continuum Mech. Thermodyn.* (2013) 1–25.

- [38] S.J. Benson, T.S. Munson, Flexible complementarity solvers for large-scale applications, *Optim. Methods Softw.* 21 (1) (2006) 155–168.
- [39] B.S. Kirk, J.W. Peterson, R.H. Stogner, G.F. Carey, *libMesh: A C++ Library for Parallel Adaptive Mesh Refinement/Coarsening Simulations*, *Eng. Comput.* 22 (3–4) (2006) 237–254.
- [40] S. Balay, W.D. Gropp, L.C. McInnes, B.F. Smith, Efficient management of parallelism in object oriented numerical software libraries, in: E. Arge, A.M. Bruaset, H.P. Langtangen (Eds.), *Modern Software Tools in Scientific Computing*, Birkhäuser Press, 1997, pp. 163–202.
- [41] S. Balay, S. Abhyankar, M.F. Adams, J. Brown, P. Brune, K. Buschelman, V. Eijkhout, W.D. Gropp, D. Kaushik, M.G. Knepley, L.C. McInnes, K. Rupp, B.F. Smith, H. Zhang, *PETSc users manual*. Technical Report ANL-95/11 - Revision 3.5, Argonne National Laboratory, 2014.
- [42] S. Burke, C. Ortner, E. Süli, An adaptive finite element approximation of a variational model of brittle fracture, *SIAM J. Numer. Anal.* 48 (3) (2010) 980–1012.
- [43] B.J. Winkler, *Traglastuntersuchungen von unbewehrten und bewehrten Betonstrukturen auf der Grundlage eines objektiven Werkstoffgesetzes für Beton* (PhD thesis), Innsbruck University Press, 2001.
- [44] G. Meschke, P. Dumstorff, Energy-based modeling of cohesive and cohesionless cracks via X-FEM, *Comput. Methods Appl. Mech. Engrg.* 196 (21–24) (2007) 2338–2357.
- [45] J.F. Unger, S. Eckardt, C. Könke, Modelling of cohesive crack growth in concrete structures with the extended finite element method, *Comput. Methods Appl. Mech. Engrg.* 196 (41–44) (2007) 4087–4100.
- [46] P. Jäger, P. Steinmann, E. Kuhl, Modeling three-dimensional crack propagation—a comparison of crack path tracking strategies, *Int. J. Numer. Methods Engrg.* 76 (9) (2008) 1328–1352.
- [47] A.R. Ingraffea, M. Grigoriu, Probabilistic fracture mechanics: a validation of predictive capability. Technical report, DTIC Document, 1990.
- [48] G. Ventura, J.X. Xu, T. Belytschko, A vector level set method and new discontinuity approximations for crack growth by efg, *Int. J. Numer. Methods Engrg.* 54 (6) (2002) 923–944.
- [49] C. Miehe, F. Welschinger, M. Hofacker, Thermodynamically consistent phase-field models of fracture: Variational principles and multi-field FE implementations, *Int. J. Numer. Methods Engrg.* 83 (10) (2010) 1273–1311.
- [50] T.N. Bittencourt, P.A. Wawrzynek, A.R. Ingraffea, J.L. Sousa, Quasi-automatic simulation of crack propagation for 2d lefm problems, *Eng. Fracture Mech.* 55 (2) (1996) 321–334.
- [51] S. Geniaut, E. Galenne, A simple method for crack growth in mixed mode with X-FEM, *Int. J. Solids Struct.* 49 (15–16) (2012) 2094–2106.
- [52] M.B. Nooru-Mohamed, *Mixed-mode fracture of concrete: an experimental approach* (Ph.D thesis), Delft University of Technology, 1992.
- [53] T.C. Gasser, G.A. Holzapfel, 3d crack propagation in unreinforced concrete.: A two-step algorithm for tracking 3d crack paths, *Comput. Methods Appl. Mech. Engrg.* 195 (37) (2006) 5198–5219.
- [54] R. De Borst, Some recent developments in computational modelling of concrete fracture, *Int. J. Fracture* 86 (1–2) (1997) 5–36.
- [55] P. Pivonka, J. Ožbolt, R. Lackner, H.A. Mang, Comparative studies of 3d-constitutive models for concrete: application to mixed-mode fracture, *Int. J. Numer. Methods Engrg.* 60 (2) (2004) 549–570.
- [56] B. Patzák, M. Jirásek, Adaptive resolution of localized damage in quasi-brittle materials, *J. Eng. Mech.* 130 (6) (2004) 720–732.
- [57] J. Bobiński, J. Tejchman, A constitutive model for concrete based on continuum theory with non-local softening coupled with extended finite element method, *Comput. Modelling Concrete Struct.* (2014) 117.
- [58] D.R. Brokenshire, *A study of torsion fracture tests*, (PhD thesis), Cardiff University, 1996.
- [59] E. Gürses, C. Miehe, A computational framework of three-dimensional configurational-force-driven brittle crack propagation, *Comput. Methods Appl. Mech. Engrg.* 198 (15) (2009) 1413–1428.
- [60] M. Baydoun, T.P. Fries, Crack propagation criteria in three dimensions using the xfem and an explicit–implicit crack description, *Int. J. Fracture* 178 (1–2) (2012) 51–70.
- [61] L. Kaczmarczyk, M.M. Nezhad, C. Pearce, Three-dimensional brittle fracture: configurational-force-driven crack propagation, *Int. J. Numer. Methods Engrg.* 97 (7) (2014) 531–550.